Journal of Alloys and Compounds 1058 (2026) 187074

Contents lists available at ScienceDirect

Journal of Alloys and Compounds

journal homepage: www.elsevier.com/locate/jalcom

Constructing a hierarchical composite of Ni@NiO core-shell nanoparticles embedded in carbon nanofibers for enhanced electrochemical performance

Shujin Hao [a,1], Bo Zhang [a,1], Qingye Zhang [a], Meng Sun [a], Lisha Zhang [a], Feiyu Diao [b], Rongsheng Cai [c,*], Yiqian Wang [a,*]

[a] College of Physics, Qingdao University, No. 308 Ningxia Road, Qingdao 266071, PR China
[b] Industrial Research Institute of Nonwovens & Technical Textiles, Shandong Center for Engineered Nonwovens, College of Textiles & Clothing, Qingdao University, No. 308 Ningxia Road, Qingdao 266071, PR China
[c] State Key Laboratory of Solid Lubrication, Lanzhou Institute of Chemical Physics, Chinese Academy of Sciences, Lanzhou 730000, PR China

ARTICLE INFO

Keywords:
Nickel oxide
Electrospinning
Core-shell nanostructure
Electrochemical performance
Synergistic effect

ABSTRACT

Nickel oxide (NiO) has garnered significant attention for its application in lithium-ion batteries (LIBs) owing to its relatively high theoretical specific capacity. However, several drawbacks such as substantial volume expansion and poor electrical conductivity during cycling hinder its practical use, leading to poor cycling and rate performances. To address these issues, a hierarchical composite material, carbon nanofibers (CNFs) loaded with Ni@NiO core-shell nanoparticles, is prepared *via* electrospinning followed by subsequent annealing at 600 °C. This composite demonstrates superior electrochemical performance compared to pure NiO, achieving a discharge specific capacity of 766.1 mAh g^{-1} after 100 cycles at 0.1 A g^{-1}. The enhanced performance is attributed to the synergistic effects of different components: NiO provides a high theoretical capacity; Ni metal accelerates the conversion reaction of NiO; both Ni and CNFs improve the electrical conductivity and cyclic stability. This study highlights the importance of material design and the synergistic effects of different components in the composite for improving the electrochemical performance of energy storage materials.

1. Introduction

Transition metal oxides, with a lithium storage mechanism through conversion reaction, have a relatively high theoretical specific capacity [1–3] and can make up for the disadvantages of conventional graphite-based anode materials [4–6]. Among them, NiO has great application potential in the field of anode materials due to its advantages such as high theoretical specific capacity (718 mAh g^{-1}) [7] and low cost [8]. However, there are several drawbacks for the NiO anode material such as large volume expansion and poor conductivity during the charging/discharging processes, resulting in poor cycling stability and rate performance, which limit its practical applications in high performance lithium-ion batteries (LIBs) [9–11].

To solve these issues, researchers have proposed various strategies to improve the electrochemical performance of NiO anode material. For example, Tian *et al.* [12] have prepared NiO/C hollow microspheres, and it shows that compounding NiO with carbon materials can improve the cycling performance of NiO anode material. Nevertheless, the other researchers have adopted a strategy of combining NiO with Ni metal to enhance its electrical conductivity [13–15]. For instance, Song *et al.* [16] have prepared NiO/Ni nanosheets by a hydrothermal method, which demonstrate that the incorporation of Ni can effectively improve the conductivity and rate performance of NiO anode material. Furthermore, Xu *et al.* [17] have synthesized carbon encapsulated Ni@NiO nanocomposites by a hydrothermal method, which exhibit an excellent electrochemical performance. From above, it can be deduced that compositing Ni/NiO with carbon materials is an effective strategy to enhance the cycling stability and rate performance of NiO anode materials [18–22]. In addition, for the above-mentioned composites, if the carbon materials are made as one-dimensional carbon nanofibers (CNFs) using an electrospinning technique, which will further enhance their electrochemical performance and is beneficial for mass production of anode materials [23–26]. To our best knowledge, only a few researchers [4] have prepared one-dimensional Ni@NiO/C nanofibers using electrospinning. However, their microstructure and electrochemical performance have not been explored until now.

* Corresponding authors.
E-mail addresses: rongshengcai@licp.cas.cn (R. Cai), yqwang@qdu.edu.cn (Y. Wang).
[1] These authors contributed to this work equally.

https://doi.org/10.1016/j.jallcom.2026.187074
Received 13 July 2025; Received in revised form 15 February 2026; Accepted 26 February 2026
Available online 27 February 2026

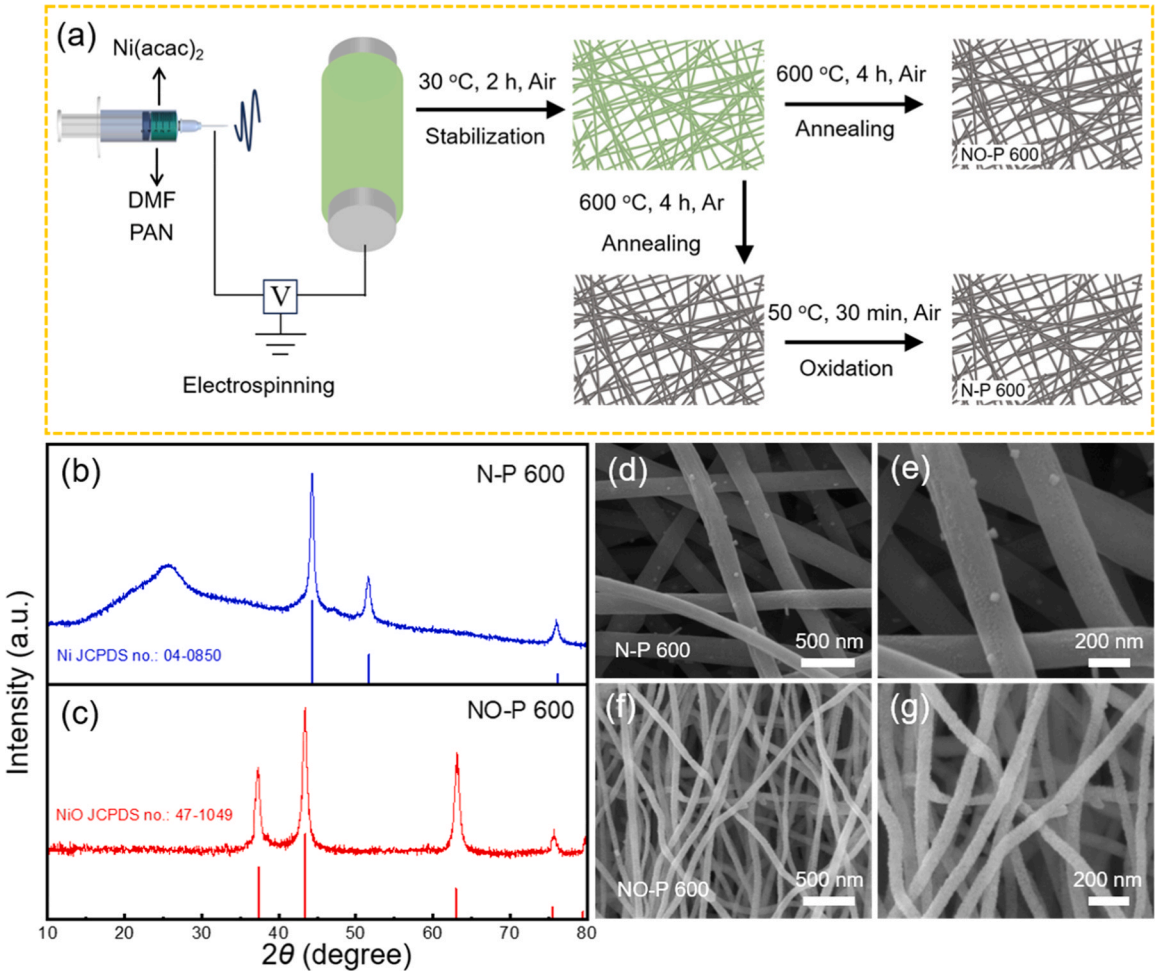

Fig. 1. (a) Schematic diagram of the preparation process for N-P 600 and NO-P 600; XRD patterns of N-P 600 (b) and NO-P 600 (c); FE-SEM images of N-P 600 (d, e) and NO-P 600 (f, g).

In this work, a hierarchical composite of CNFs loaded with core-shell Ni@NiO nanoparticles has been prepared by electrospinning. The microstructure and electrochemical performance of this composite are systematically investigated. Compared to pure NiO nanofibers, this composite demonstrates superior rate performance and cycling stability.

2. Experimental

2.1. Materials synthesis

Polyacrylonitrile (PAN, average Mw. 150,000) and nickel acetylacetonate [$Ni(acac)_2$, 98%] were dissolved in the N, N-Dimethylformamide (DMF) solvent. Then it was stirred at 25 °C for 6 h until a uniform and viscous spinning solution was produced. Afterwards, the solution was spun into a fiber membrane by electrospinning, and the detailed electrospinning parameters can be found elsewhere [27]. The fiber membrane was then dried in the air at 30 °C for 2 h to allow the excess DMF to evaporate [28]. Subsequently, it was annealed in air and argon atmospheres at 600 °C for 4 h, respectively. The product obtained in the air was named as NO-P 600. The annealing product in the argon atmosphere underwent further oxidation treatment at 50 °C for 30 min in the air, and the final product was named as N-P 600. The preparation process for both NO-P 600 and N-P 600 is shown in Fig. 1a, respectively.

2.2. Materials characterization

The crystal structure of the products was analyzed by X-ray diffractometer (XRD, Bruker D8 Advance) with Cu-Kα radiation (λ = 1.5406 Å). Then, the morphologies of the products were observed by field-emission scanning electron microscope (FE-SEM, Sigma 500) operated at 20 kV. Bright field (BF) and high-resolution transmission electron microscopy (HRTEM) images were acquired with a transmission electron microscope (TEM, JEOL JEM 2100 F) operated at 200 kV. High-angle annular dark field (HAADF) imaging was conducted on a scanning transmission electron microscope (STEM, Thermo Fisher Spectra 300). The chemical composition and valence states of the elements were determined by energy dispersive X-ray spectrometer (EDS, Oxford INCAx-Sight6427) and X-ray photoelectron spectroscopy (XPS, Thermo Scientific K-Alpha$^+$), respectively.

2.3. Measurement of electrochemical properties

Both N-P 600 and NO-P 600 were ground into powder, and mixed with acetylene black and polyvinylidene fluoride in a mass ratio of 7:2:1, respectively. N-Methylpyrrolidone (NMP) was then added as a solvent, and the mixture was ground to form a slurry. This slurry was uniformly coated onto copper foil, dried under vacuum for 12 h, and pressed into electrode sheets. Then, the assembly process was performed in a glove box filled with high-purity argon. An electrolyte consisting of a 1 M $LiPF_6$ solution mixed with ethylene carbonate (EC), dimethyl carbonate (DMC), and diethyl carbonate (DEC) in a volumetric ratio of 1:1:1 was employed. The lithium foil was used as the counter electrode and Celgard-2500 as the separator to prepare the CR2025 button half-cell. The cycling stability and rate performance were assessed using a

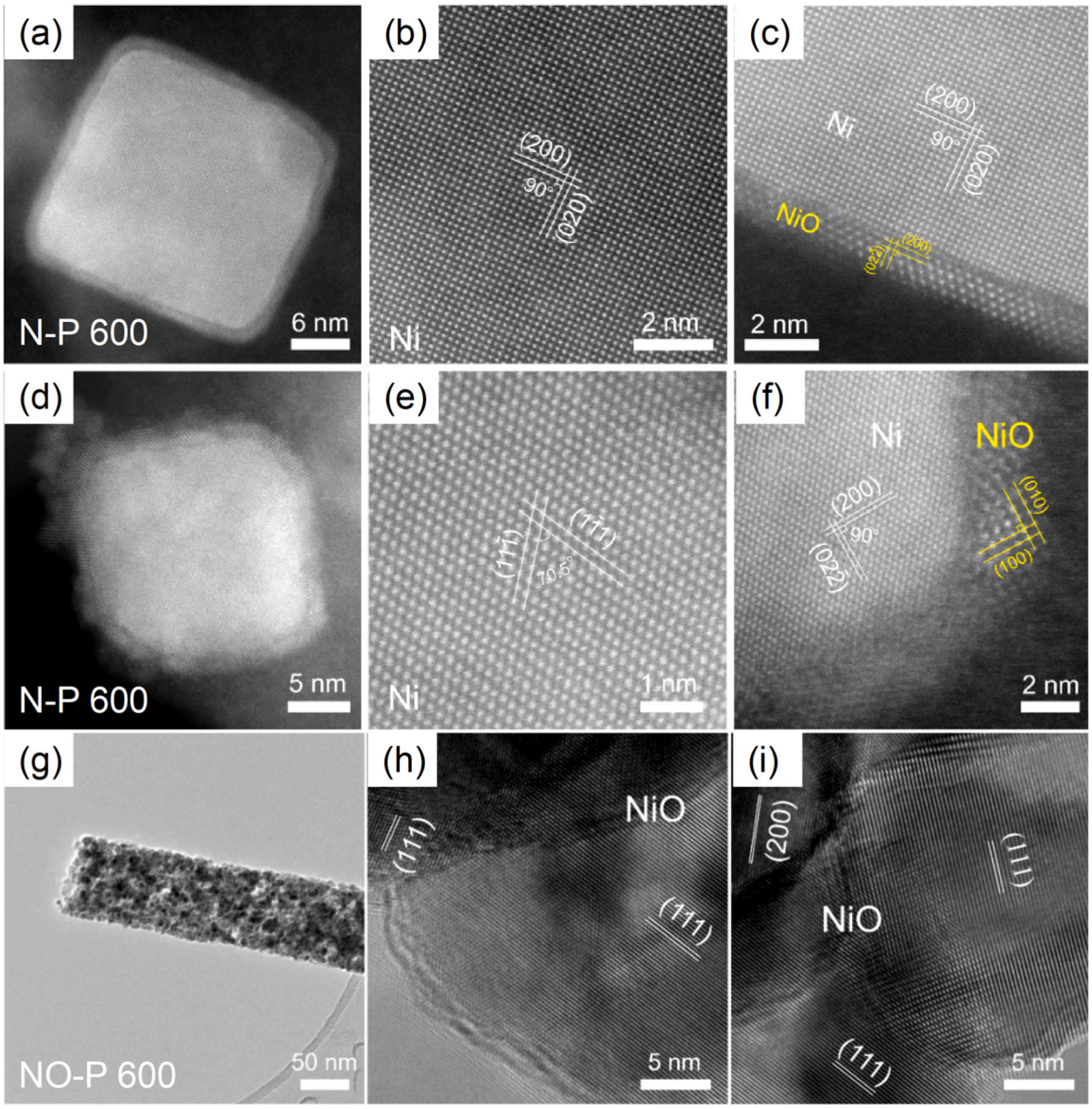

Fig. 2. STEM images of the nanoparticles in the N-P 600: (a, d) Low-magnification STEM image of an individual nanoparticle; HRSTEM images of the central region (b) and edge region (c) of the nanoparticle in (a); HRSTEM images of the central region (e) and edge region (f) of the nanoparticle in (d); (g) BF TEM image of a single nanofiber in the NO-P 600; (h,i) HRTEM images of nanoparticles in the NO-P 600.

LAND CT2001 battery testing system, with a voltage range of 0.01–3.00 V. Cyclic voltammetry (CV) and electrochemical impedance spectroscopy (EIS) measurements were conducted on a Metrohm Autolab electrochemical workstation (PGSTAT 302 N). Specifically, CV curves were obtained at a scan rate of 0.3 mV/s within a potential range of 0.01–3.00 V, and EIS spectra were recorded at a frequency range from 100 kHz to 0.01 Hz with a disturbance amplitude of 5 mV.

3. Results and discussion

To explore the crystal structures of the products, XRD analysis was employed. Fig. 1b shows the XRD pattern of N-P 600. In Fig. 1b, there is a relatively wide diffraction peak at approximately 26°, which originates from amorphous carbon, indicating that a certain amount of carbon exists in the N-P 600. Meanwhile, there are three obvious diffraction peaks at 44.5°, 51.8° and 76.4°, corresponding to the (111), (200) and (220) crystal planes of cubic Ni (JCPDS no.: 04–0850, a = 3.524 Å), respectively, which indicates presence of metallic Ni in the N-P 600 [29]. Fig. 1c shows the XRD pattern of NO-P 600. The diffraction peaks observed at 37.2°, 43.3°, 62.9° and 75.4° correspond to the (111), (200), (220) and (311) crystal planes of cubic NiO (JCPDS no.: 47–1049, a = 4.177 Å), respectively, and no other diffraction peaks are observed in the XRD pattern, indicating that the NO-P 600 is composed of NiO. To further investigate the morphology of N-P 600 and NO-P 600, FE-SEM examinations were carried out. Fig. 1d and e present the FE-SEM images of N-P 600, from which it can be observed that N-P 600 exhibits an evident morphology of uniform nanofibers. In addition, many nanofibers interweave with each other, forming a loose 3D network structure, which can provide ample space and abundant active sites. This unique structure not only facilitates the penetration of the electrolyte but also increases the contact area between the electrode and the electrolyte, thereby enhancing the transport rate of lithium ions and providing essential conditions for rapid charging and discharging of LIBs [30]. As shown in Fig. 1f and g, the morphology of NO-P 600 is manifested by nanoparticle-constituted fibers, which have relatively small diameters and contain plenty of pores. This is ascribed to the fact that a large amount of carbon in the fibers is consumed during the annealing process in air, causing the fibers to shrink.

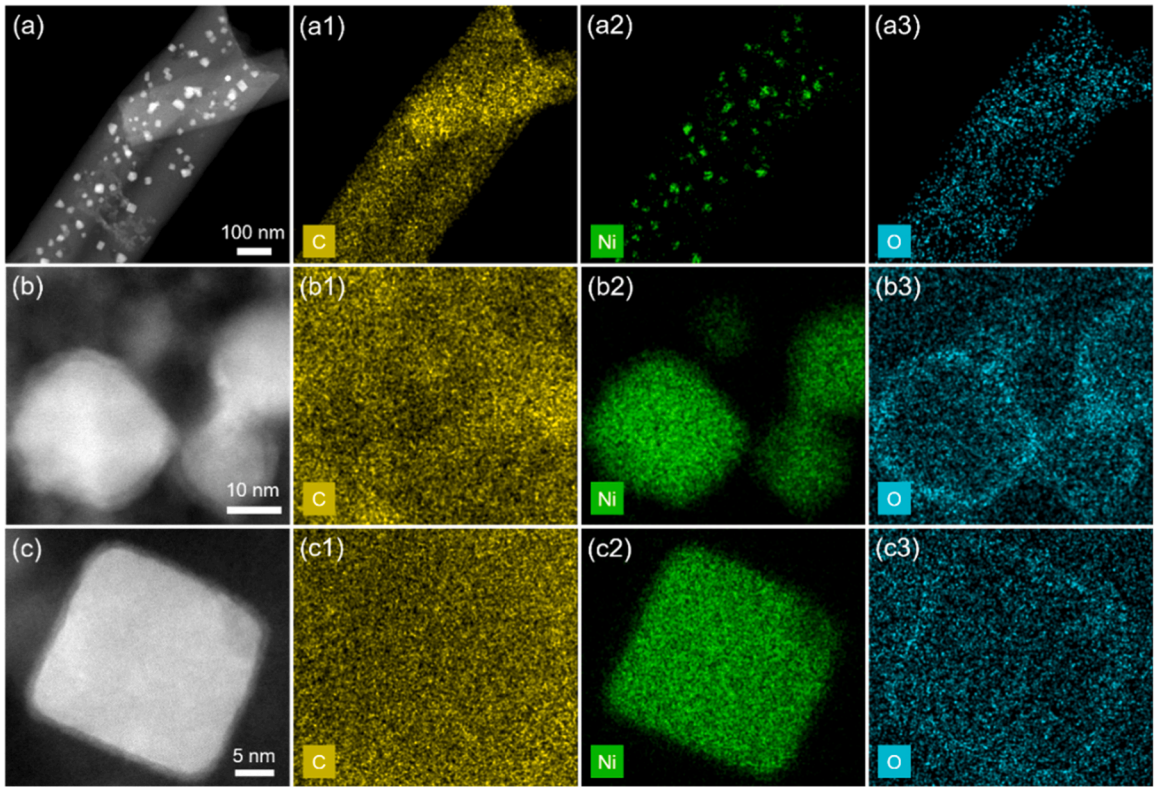

Fig. 3. HAADF-STEM images and elemental mapping images of N-P 600: (a) several nanofibers, (b) several nanoparticles, (c) individual nanoparticle.

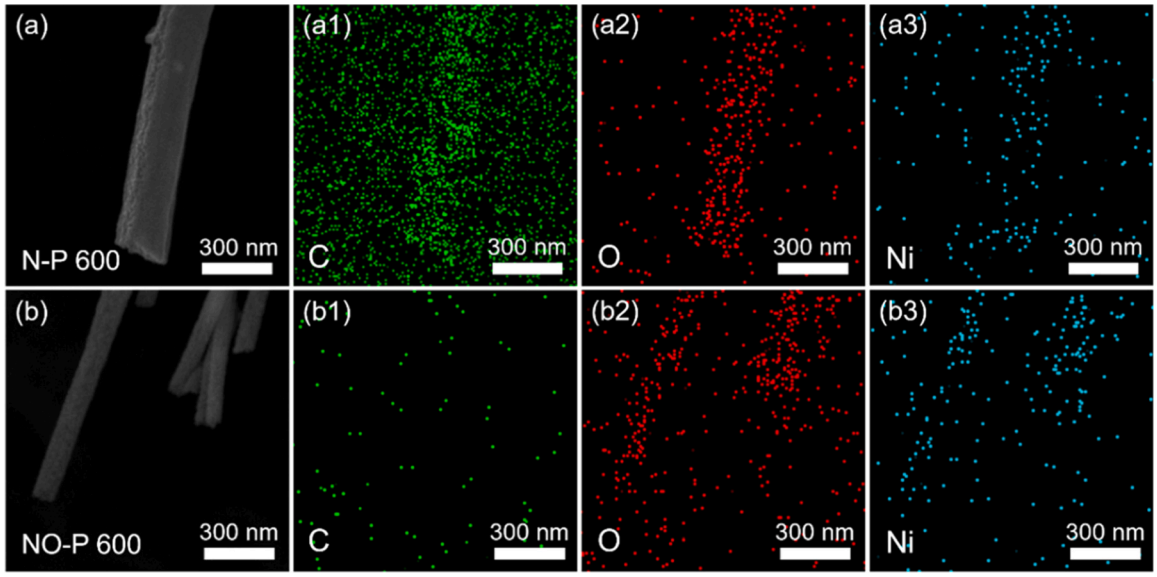

Fig. 4. SEM images and EDS elemental mappings of (a) N-P 600 and (b) NO-P 600.

Table 1
Quantification results of EDS for N-P 600 and NO-P 600.

Membrane	C (at%)	O (at%)	Ni (at%)
N-P 600	83.7	10.3	6.0
NO-P 600	5.7	47.6	46.7

Fig. 2a and d show typical low-magnification STEM images of two individual nanoparticles with a square shape in the N-P 600. It can be clearly seen that the central regions have much brighter contrast than the edge regions, suggesting that the nanoparticles in the N-P 600 might contain two phases with different chemical compositions. To further clarify the different phases in the nanoparticle and their orientation relationships, high-resolution STEM (HRSTEM) examinations were performed. Fig. 2b presents [001] zone-axis HRSTEM image of the central region of the nanoparticle in Fig. 2a. The lattice spacings of two crystal planes are measured to be 2.08 Å with an angle of 90°, which is consistent with the {200} crystal planes of the cubic Ni [31]. Fig. 2c shows a typical HRSTEM image of the edge region of the nanoparticle in Fig. 2a. For the upper part of this image, it can be indexed as [001]

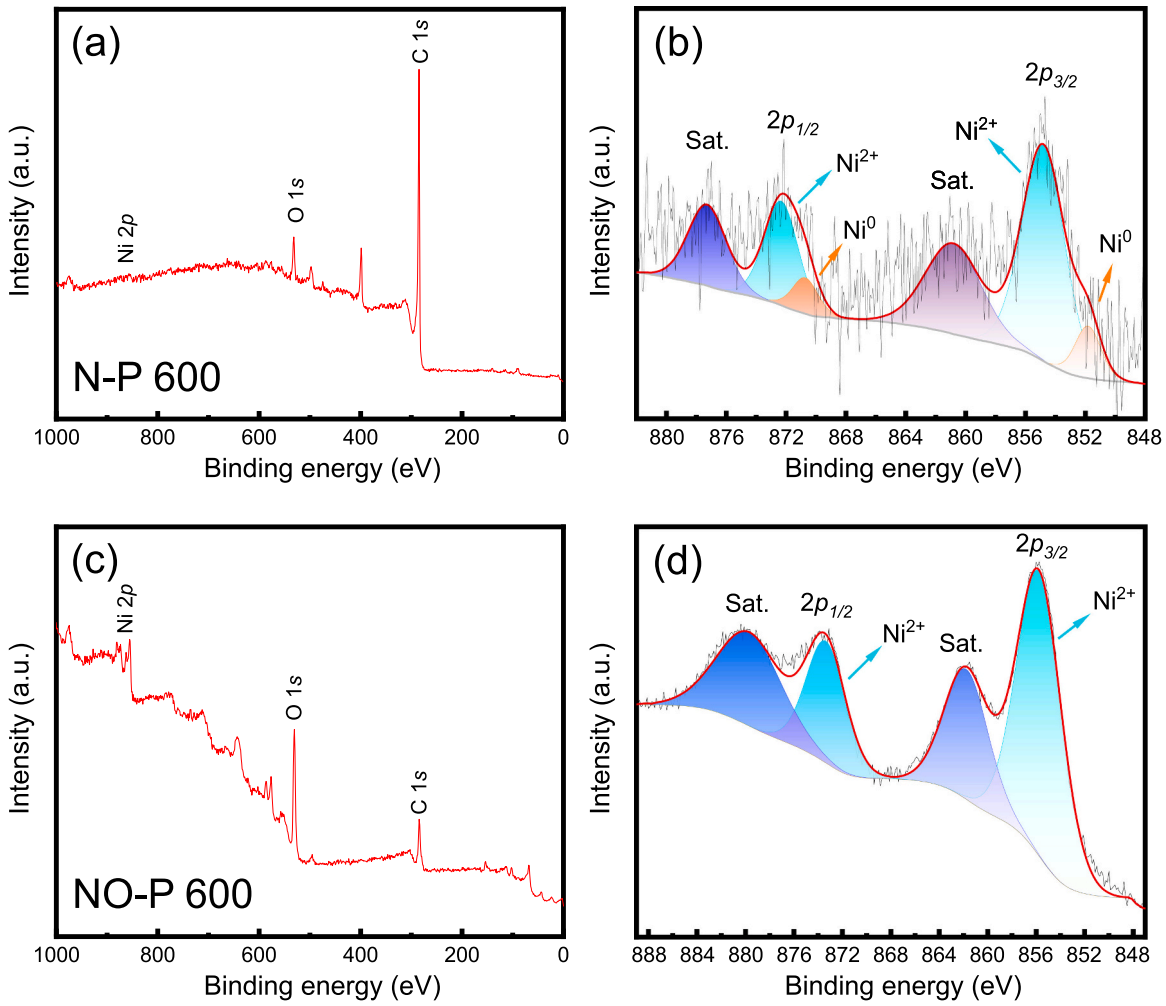

Fig. 5. XPS spectra of N-P 600: (a) Full XPS spectrum, (b) XPS spectra of Ni 2*p*. XPS spectra of NO-P 600: (c) Full XPS spectrum, (d) XPS spectra of Ni 2*p*.

zone-axis of cubic Ni with two perpendicular planes of (200) and (020). For the lower part of this image, it can be indexed as [011] zone-axis of cubic NiO, where the interplanar spacings of (02$\bar{2}$) and (200) are measured to be 1.48 Å and 2.09 Å [32]. The orientation relationships for Ni and NiO in Fig. 2c are described as follows.

$(200)_{Ni}$ // $(200)_{NiO}$

(020)Ni // (02$\bar{2}$)NiO

$[001]_{Ni}$ // $[011]_{NiO}$ (1)

Fig. 2e is the [011] zone-axis HRSTEM image of the central region of the nanoparticle in Fig. 2d. The interplanar spacings are measured to be 2.03 Å and the angle of the two planes is 70.5°, corresponding to the (1$\bar{1}$1) and (11$\bar{1}$) planes of Ni, respectively. Fig. 2f displays a HRSTEM image of the edge region of the nanoparticle in Fig. 2d. For the left part of this image, it can be indexed as [011] zone-axis of cubic Ni with two perpendicular planes of (02$\bar{2}$) and (200). For the right part of this image, it can be indexed as [001] zone-axis of cubic NiO, where the interplanar spacings of {100} planes are measured to be 4.18 Å [33,34]. The orientation relationships for Ni and NiO in Fig. 2f are described as follows.

$(200)_{Ni}$ // $(200)_{NiO}$

(02$\bar{2}$)Ni // (020)NiO

$[011]_{Ni}$ // $[001]_{NiO}$ (2)

From the above analysis, it can be concluded that the nanoparticles in N-P 600 possess a Ni@NiO core-shell heterostructure, where Ni and NiO have two reversible orientation relationships, reflecting a good epitaxial growth of NiO on Ni. From the STEM examinations, it can be clearly seen that the NiO layers in the nanoparticles are very thin, which explains why NiO is not detected in the N-P 600 using XRD analysis. To further clarify the nature of nanoparticles constituting the nanofibers in the NO-P 600, extensive TEM examinations were carried out. Fig. 2g shows a typical BF TEM image of a single nanofiber in the NO-P 600. From Fig. 2g, it can be seen that this fiber is composed of many nanoparticles, which is consistent with our SEM observations. Fig. 2h and i show typical HRTEM images of several nanoparticles in the single nanofiber of the NO-P 600.

To further prove the formation of Ni@NiO core-shell structure in the N-P 600, EDS elemental mappings were conducted. As shown in Fig. 3a, it can be clearly observed that many square-shaped nanoparticles are loaded on the nanofibers with a uniform distribution of C element throughout the fiber matrix, further confirming that the N-P 600 consists of CNFs decorated with nanoparticles. Contrary to the C element, the O element exhibits a non-uniform distribution, with a significantly high concentration in the region with a pile-up of nanoparticles. Fig. 3b presents a typical STEM image and elemental mappings of several nanoparticles, revealing that the carbon content is relatively low within each nanoparticle. Notably, O element is preferentially distributed around the Ni, directly evidencing the formation of the core-shell structure. Fig. 3c is a typical STEM image and elemental mappings of a single nanoparticle, clearly demonstrating that metallic Ni is

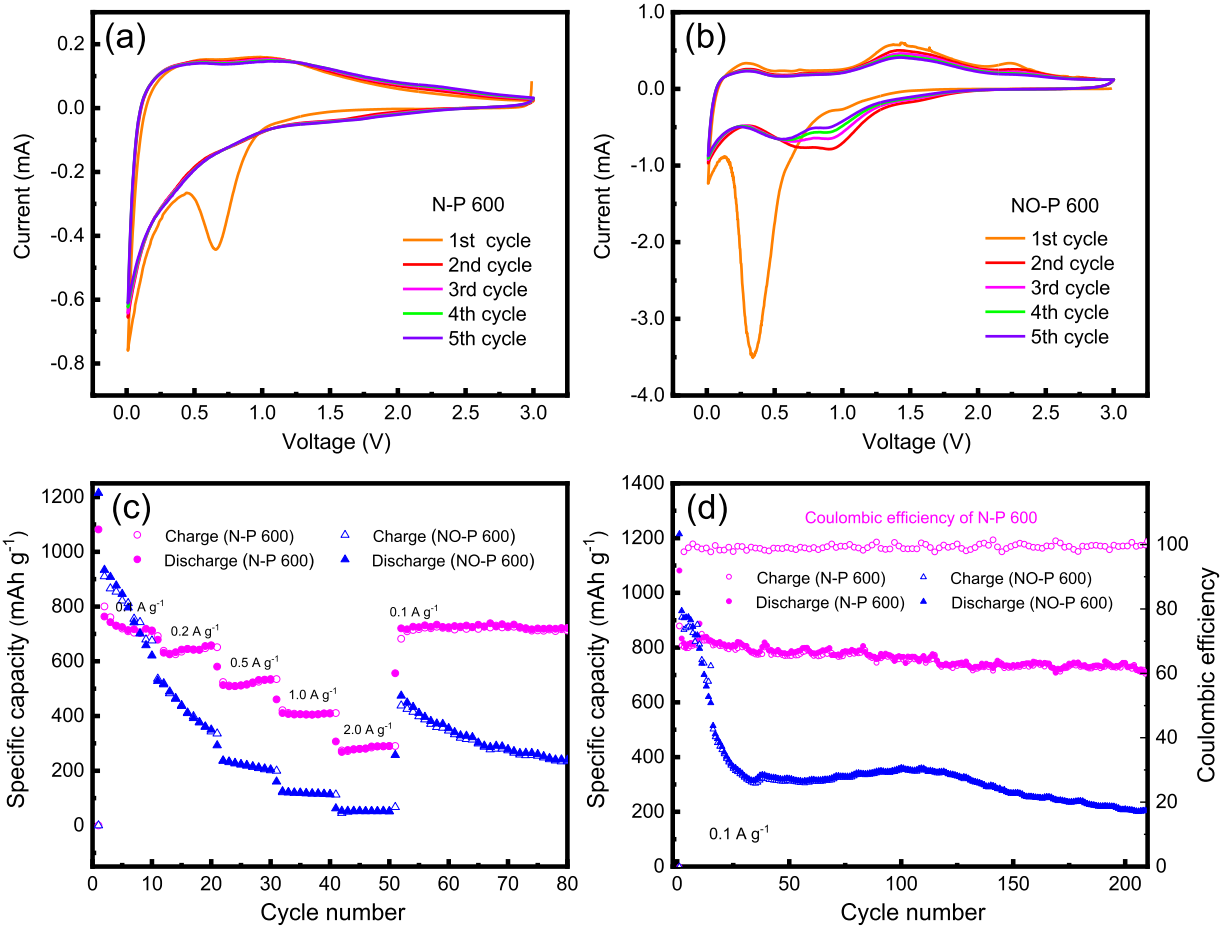

Fig. 6. CV curves of the first five cycles at a scanning rate of 0.3 mV s^{-1}: (a) N-P 600; (b) NO-P 600. (c) Rate performance of N-P 600 and NO-P 600 electrodes. (d) Cycling performance of N-P 600 and NO-P 600 electrodes at a current density of 0.1 A g^{-1}.

Table 2
Summary of electrochemical properties for the NiO-based anode materials.

Anode material	Current density (mA g^{-1})	Cycle number	Reversible capacity (mAh g^{-1})	Ref.
NiO microspheres	100	50	612	[60]
Ni@NiO nanowires	100	100	697.9	[61]
NiO microspheres	70	50	550	[62]
C/Ni-NiO nanofibers	50	35	515	[63]
Egg shell-yolk NiO/C	100	100	625.3	[64]
MnO/C/NiO	100	200	352.9	[65]
N-P 600	100	200	730.8	**This work**

encapsulated by a thin oxygen-rich layer. Combining with the HRSTEM examinations, the O element surrounding the square-shaped nanoparticles is attributed to the formation of NiO. Thus, it is further proved that in the N-P 600, CNFs are loaded with many nanoparticles possessing a Ni@NiO core-shell structure.

Through measuring the interplanar spacing of the particles in these images, all the particles constituting the fibers are identified as NiO. Therefore, NO-P 600 consists of nanofibers formed by NiO nanoparticles, which is consistent with our XRD analysis results. In addition, the distributions of different elements in the N-P 600 and NO-P 600 were examined using EDS elemental mappings, as depicted in Fig. 4. From Fig. 4b and c, it can be seen that three elements (C, O and Ni) are uniformly distributed in the N-P 600, with relatively high carbon content. In contrast, only O and Ni elements are uniformly distributed in the NO-P 600 with very low carbon content. To explore the chemical composition of N-P 600 and NO-P 600, the atomic ratios of various elements (C, O and Ni) were presented in Table 1. For the N-P 600, the carbon content is high, further confirming that the product is carbon nanofibers. In contrast, the NO-P 600 is primarily composed of Ni and O.

To gain further insight into the valence states of Ni in the products, N-P 600 and NO-P 600 were investigated using XPS. Fig. 5a presents the full XPS spectrum of the N-P 600, in which the C 1 s peak exhibits a relatively high intensity, indicating a high content of carbon in the N-P 600. Fig. 5b is typical XPS spectra of Ni 2*p* in the N-P 600 with two peaks located at 870 eV and 852 eV, corresponding to Ni $2p_{1/2}$ and Ni $2p_{3/2}$ of Ni^0. Meanwhile, the peaks located at 873 eV and 855 eV correspond to the Ni $2p_{1/2}$ and Ni $2p_{3/2}$ of Ni^{2+}, respectively [35]. This indicates that the Ni element in the N-P 600 exists simultaneously in the form of Ni and NiO [36,37]. In Fig. 5c, the XPS full spectrum of the NO-P 600 demonstrates that the carbon content is negligible. Fig. 5d displays typical spectra of Ni 2*p* for the NO-P 600 with two peaks located at 873 eV and 855 eV, which are assigned to Ni $2p_{1/2}$ and Ni $2p_{3/2}$ of NiO, respectively.

To explore the electrochemical performance of the N-P 600 and NO-P 600, Fig. 6a and b show the CV curves of the first five cycles for the N-P 600 and NO-P 600 electrodes at a scanning rate of 0.3 mV s^{-1}, respectively. For the N-P 600 electrode, during the initial cathodic scanning process (Fig. 6a), the reduction peak located at 0.67 V is attributed to the formation a solid electrolyte interface (SEI) film [38]. Meanwhile, no obvious oxidation peak is observed during the initial anodic scanning process, which results from the high carbon content in the fibers. From the second to the fifth cycle, the CV curves are highly overlapped,

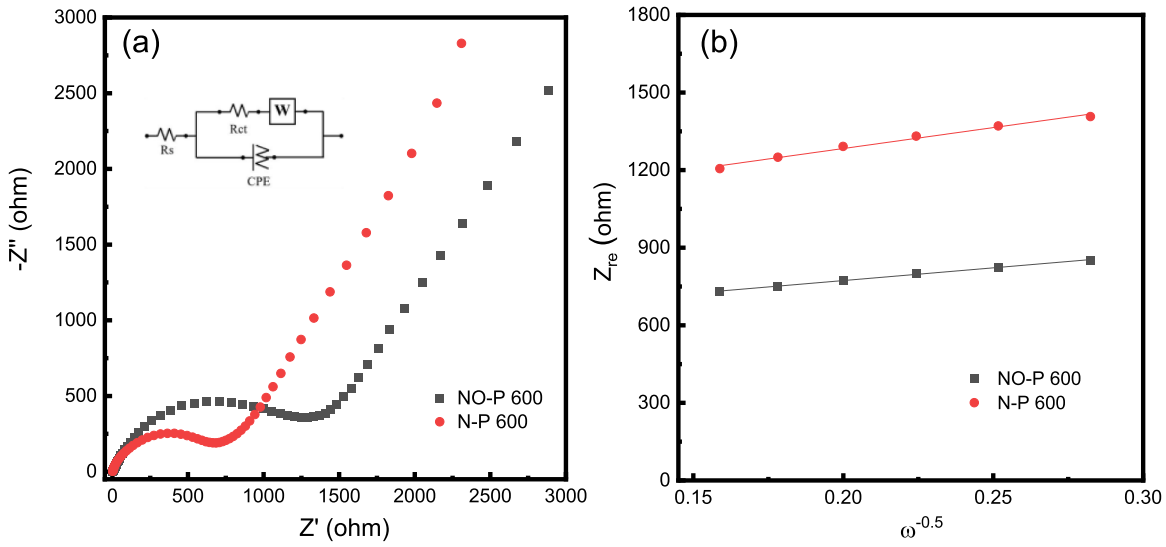

Fig. 7. (a) EIS spectra of the N-P 600 and NO-P 600 electrodes; The inset shows the equivalent circuit diagram for fitting impedance spectra. (b) Z_{re} and $\omega^{-0.5}$ fitting plots for the N-P 600 and NO-P 600 electrodes.

indicating that N-P 600 has an excellent cycling stability. Based on the above analysis, the N-P 600 electrode has an outstanding structural stability during the cycling, which enables highly reversible intercalation/deintercalation of Li^+ ions and consequently ensures excellent cycling stability [39–41]. During the initial cathodic scanning process (Fig. 6b) of the NO-P 600 electrode, a reduction peak is found at 0.7 V, corresponding to the reduction of Ni^{2+} to Ni^0. The strong reduction peak located at 0.3 V signifies the formation of the SEI film. During the initial anodic scanning process, the oxidation peak located at 1.3 V corresponds to the oxidation of Ni^0 to Ni^{2+}. In addition, the CV curves for the NO-P 600 electrode do not overlap after the second cycle, indicating a poor cycling stability. Fig. 6c illustrates the rate performance of the N-P 600 and NO-P 600 electrodes at the different current densities. Compared with the NO-P 600 electrode, the N-P 600 electrode shows an excellent rate performance with average discharge specific capacities of 761.1, 645.4, 525.9, 412.4 and 284.5 mAh g^{-1} at current densities of 0.1, 0.2, 0.5, 1.0 and 2.0 A g^{-1}, respectively. When the current density recovers from 2.0 A g^{-1} to 0.1 A g^{-1}, the discharge specific capacities of the N-P 600 and NO-P 600 electrodes remain 725.7 and 376.1 mAh g^{-1} after 80 cycles, respectively. To investigate their cycling performance, N-P 600 and NO-P 600 electrodes were tested for 200 cycles at a current density of 0.1 A g^{-1}, as shown in Fig. 6d. The initial discharge specific capacity of the NO-P 600 electrode is 1215.1 mAh g^{-1}, which is higher than that of the N-P 600 electrode (1081.6 mAh g^{-1}). After 200 cycles, the discharge specific capacity of the N-P 600 and NO-P 600 electrodes maintains 730.8 mAh g^{-1} and 209.58 mAh g^{-1} with a capacity retention rate of 67.6% and 17.2%, respectively. Overall, the N-P 600 electrode exhibits excellent rate performance and cycling stability, which is attributed to the synergistic effects between CNFs and Ni@NiO nanoparticles: NiO has a high theoretical specific capacity; Ni and CNFs contribute to enhanced cycling stability and rate performance of the anode material [42]. Table 2 summarizes the electrochemical performance of NiO-based anodes for LIBs in the previous literature, showing that the N-P 600 anode in this work has an excellent electrochemical performance.

EIS measurements were carried out to further explore the electrochemical reaction kinetics of the N-P 600 and NO-P 600 electrodes. Fig. 7a shows the EIS spectra and the corresponding equivalent circuit diagrams of N-P 600 and NO-P 600 electrodes. In the equivalent circuit diagram, W, CPE, *Rs* and *Rct* stand for the Warburg impedance, constant phase element, electrolyte impedance and charge-transfer impedance, respectively [10]. In the high-frequency region of the EIS spectrum, *Rct* is represented by the semicircle diameter, and *Rs* is denoted by the impedance at the starting point of the semicircle. After fitting the high-frequency region, for the N-P 600 and NO-P 600 electrodes, the *Rct* values are 664.2 Ω and 1248.2 Ω, and the *Rs* values are 2.5 and 7.4 Ω, respectively. The lower values of *Rct* and *Rs* for the N-P 600 are primarily attributed to the enhanced conductivity induced by metallic Ni and CNFs [43]. In the low-frequency region of the EIS spectrum, the inclined line is associated with the Li^+ diffusion coefficient (D_{Li}) of the electrode, which can be calculated by the equations [44–46] as follows.

$$D_{Li} = \frac{R^2T^2}{2A^2n^4F^4C^2\sigma^2} \quad (3)$$

$$Z' = R_s + R_{ct} + \sigma\omega^{-0.5} \quad (4)$$

where *n* is the number of electrons transferred per mole of the substance. *C* is the concentration of Li^+ in the LIBs, and the electrode area *A* is 1.54×10^{-4} m^2. The other parameters are available in the Ref. [47]. Fig. 7b shows the fitting diagrams of Z_{re} and $\omega^{-0.5}$ for the N-P 600 and NO-P 600 electrodes. The σ values are calculated to be 17.1 and 35.4 Ω $s^{-0.5}$ for the N-P 600 and NO-P 600, respectively. Furthermore, the D_{Li} values are determined to be 3.6×10^{-16} and 1.5×10^{-15} cm^2 s^{-1} for the N-P 600 and NO-P 600 electrodes, respectively. It can be seen that the NO-P 600 electrode has a higher lithium-ion diffusion capacity than the N-P 600, suggesting that its porous structure facilitates the lithium-ion transport. The two samples show similar Li+ diffusion rates. Metallic Ni and carbon nanofibers in N-P 600 improve conductivity and lead to lower charge transfer resistance, while NO-P 600 is composed of nanoparticles with abundant interspaces that facilitate Li^+ diffusion, resulting in similar diffusion rates [48–59].

4. Conclusions

A hierarchical composite of Ni@NiO core-shell nanoparticles embedded in carbon nanofibers has been prepared by electrospinning followed by subsequent annealing in argon at 600 °C. For the core-shell nanoparticles, NiO shows a good epitaxial growth on Ni, with two reversible orientation relationships between Ni and NiO. When the composite is used as anode material for LIBs, it demonstrates superior rate performance and cycling stability. The enhanced electrochemical performance is primarily attributed to the synergistic interactions between the three components: NiO contributes a high theoretical specific capacity; the metal Ni with catalytic effect can promote the conversion

reaction of NiO; both Ni and CNFs enhance the cycling stability and electrical conductivity of the anode. This work presents a reliable strategy to utilize the synergistic effects among different components in a hierarchical composite anode, offering a promising route for the development of high-performance LIBs.

CRediT authorship contribution statement

Shujin Hao: Writing – original draft, Investigation, Formal analysis. **Bo Zhang:** Investigation, Formal analysis. **Qingye Zhang:** Writing – review & editing, Formal analysis. **Rongsheng Cai:** Writing – review & editing, Methodology, Formal analysis. **Yiqian Wang:** Writing – review & editing, Supervision, Funding acquisition, Conceptualization. **Meng Sun:** Validation, Formal analysis. **Lisha Zhang:** Validation, Formal analysis. **Feiyu Diao:** Writing – review & editing, Formal analysis.

Declaration of Competing Interest

There are no conflicts to declare.

Acknowledgments

The authors gratefully acknowledge the financial support from the High-end Foreign Experts Programs of the Ministry of Science and Technology, China (Grant Nos.: G2022025015L, G2022025016L, H20250033), and Shandong Province "Double-Hundred Talent Plan" Program (Grant No.: WST2018006). Y. Q. Wang acknowledges the support from the Taishan Scholar Program of Shandong Province, China, the Qingdao International Center of Semiconductor Photoelectric Nanomaterials, and the Shandong Provincial University Key Laboratory of Optoelectrical Material Physics and Devices.

Data availability

Data will be made available on request.

References

[1] M.M. Thackeray, C. Wolverton, E.D. Isaacs, Electrical energy storage for transportation-approaching the limits of, and going beyond, lithium-ion batteries, Energy Environ. Sci. 5 (2012) 7854, https://doi.org/10.1039/C2EE21892E.
[2] H. Cheng, J.G. Shapter, Y. Li, G. Gao, Recent progress of advanced anode materials of lithium-ion batteries, J. Energy Chem. 57 (2021) 451–468, https://doi.org/10.1016/j.jechem, 2020.08.056.
[3] S. Behera, S. Ippili, V. Jella, N.Y. Kim, S.C. Jang, J.W. Jung, S.G. Yoon, H.S. Kim, Confluence of ZnO and PTFE binder for enhancing performance of thin-film lithium-ion batteries, Energy Environ. Mater. 7 (2024) e12734, https://doi.org/10.1002/eem2.12734.
[4] Y.Q. Shen, Y.P. Wei, J. Li, Y.C. Zhang, B. Li, X.F. Lu, B.H. Ji, P.Z. Yan, X.Y. Du, Fabrication of microwave absorbing Ni/NiO/C nanofibers with robust superhydrophobic properties by electrospinning, J. Mater. Sci. Mater. Electron. 31 (2020) 226–238, https://doi.org/10.1007/s10854-019-02462-y.
[5] Y. Liu, H. Shi, Z.-S. Wu, Recent status, key strategies and challenging perspectives of fast-charging graphite anodes for lithium-ion batteries, Energy Environ. Sci. 16 (2023) 4834–4871, https://doi.org/10.1039/D3EE02213G.
[6] W. Zhao, C. Zhao, H. Wu, L. Li, C. Zhang, Progress, challenge and perspective of graphite-based anode materials for lithium batteries: a review, J. Energy Storage 81 (2024) 110409, https://doi.org/10.1016/j.est.2023.110409.
[7] S.C. Sekhar, G. Nagaraju, J.S. Yu, High-performance pouch-type hybrid supercapacitor based on hierarchical NiO-Co_3O_4-NiO composite nanoarchitectures as an advanced electrode material, Nano Energy 48 (2018) 81–92, https://doi.org/10.1016/j.nanoen.2018.03.037.
[8] J. Liang, X. Liu, T. Zhang, K. Yu, C. Liang, Hemp straw carbon and Ni/NiO embedded structure composites as anode materials for lithium ion batteries, J. Alloy. Compd. 889 (2021) 161776, https://doi.org/10.1016/j.jallcom.2021.161776.
[9] Y.J. Mai, S.J. Shi, D. Zhang, Y. Lu, C.D. Gu, J.P. Tu, NiO-graphene hybrid as an anode material for lithium ion batteries, J. Power Sources 204 (2012) 155–161, https://doi.org/10.1016/j, jpowsour.2011.12.038.
[10] Y.F. Zhang, M.H. Xie, Y.B. He, Y.M. Zhang, L.D. Liu, T.Q. Hao, Y. Ma, Y.F. Shi, Z. J. Sun, N. Liu, Z.J. Zhang, Hybrid NiO/Co_3O_4 nanoflowers as high-performance anode materials for lithium-ion batteries (.), Chem. Eng. J. 420 (2021) 130469, https://doi.org/10.1016/j.cej. . 2021.130469..
[11] B. Zhang, F. Xie, S.J. Hao, M. Sun, F.Y. Diao, R.S. Cai, Y.Q. Wang, Effect of annealing atmosphere on the phase composition and electrochemical properties of iron-oxide-based electrospun nanofibers (.), J. Energy Storage 124 (2025) 116851, https://doi.org/10.1016/j. . est.2025.116851..
[12] J. Tian, Q. Shao, X. Dong, J. Zheng, D. Pan, X. Zhang, H. Cao, L. Hao, J. Liu, X. Mai, Z. Guo, Bio-template synthesized NiO/C hollow microspheres with enhanced Li-ion battery electrochemical performance, Electrochim. Acta 261 (2018) 236–245, https://doi.org/10.1016/j, electacta.2017.12.094.
[13] I. Rakhimbek, N. Baikalov, A. Konarov, A. Mentbayeva, Y. Zhang, Z. Bakenov, Nickel and nickel oxide nanoparticle-embedded functional carbon nanofibers for lithium sulfur batteries, Nanoscale Adv. 6 (2024) 578–589, https://doi.org/10.1039/d3na00785e.
[14] E. Beletskii, M. Pinchuk, V. Snetov, A. Dyachenko, A. Volkov, E. Savelev, V. Romanovski, Simple solution plasma synthesis of Ni@NiO as high-performance anode material for lithium-ion batteries application, e202400427, ChemPlusChem 89 (2024), https://doi.org/10.1002/cplu.202400427.
[15] J. Wang, X. Guo, X. Du, J. Liang, J. Wu, G. Zhao, X. Li, S. Gui, F. Zheng, J. Zhao, C. Xu, D. Wang, H. Yang, B. Zhang, Y. Zhu, Revealing the complex lithiation pathways and kinetics of core-shell NiO@CuO electrode, Energy Storage Mater. 51 (2022) 11–18, https://doi.org/10.1016/j.ensm.2022.06.022.
[16] R. Song, N.S. Zhang, H. Dong, P. Wang, H. Ding, J. Wang, S.Y. Li, Self-standing three-dimensional porous NiO/Ni anode materials for high-areal capacity lithium storage, Mater. Des. 215 (2022) 110448, https://doi.org/10.1016/j.matdes.2022.110448.
[17] D. Xu, C. Mu, B. Wang, J. Xiang, W. Ruan, F. Wen, X. Du, Z. Liu, Y. Tian, Fabrication of multifunctional carbon encapsulated Ni@NiO nanocomposites for oxygen reduction, oxygen evolution and lithium-ion battery anode materials, Sci. China Mater. 60 (2017) 947–954, https://doi.org/10.1007/s40843-017-9094-5.
[18] L. Wang, C. Shi, L. Wang, L. Pan, X. Zhang, J. Zou, Rational design, synthesis, adsorption principles and applications of metal oxide adsorbents: a review, Nanoscale 12 (2020) 4790–4815, https://doi.org/10.1039/C9NR09274A.
[19] Q. Hu, F. Zhu, R. Li, M. Du, Y. Meng, Y. Zhang, Facile synthesis of Ni-NiO/C anode with enhanced lithium storage and long cycling life, Ionics 25 (2019) 5759–5767, https://doi.org/10.1007/s11581-019-03130-1.
[20] H.W. Lai, Q. Wu, J. Zhao, L.M. Shang, H. Li, R.C. Che, Z.Y. Lyu, J.F. Xiong, L. J. Yang, X.Z. Wang, Z. Hu, Mesostructured NiO/Ni composites for high-performance electrochemical energy storage, Energy Environ. Sci. 9 (2016) 2053–2060, https://doi.org/10.1039/C6EE00603E.
[21] J. Pu, T. Wang, X.M. Zhu, Y. Tan, L.L. Gao, J.X. Chen, J.R. Huang, Z.H. Wang, Multifunctional Ni/NiO heterostructure nanoparticles doped carbon nanorods modified separator for enhancing Li-S battery performance, Electrochim. Acta 435 (2022) 141396, https://doi.org/10.1016/j.electacta.2022.141396.
[22] X. Sheng, T. Li, M. Sun, G. Liu, Q. Zhang, Z. Ling, S. Gao, F. Diao, J. Zhang, F. Rosei, Y.Q. Wang, Flexible electrospun iron compounds/carbon fibers: phase transformation and electrochemical properties, Electrochim. Acta 407 (2022) 139892, https://doi.org/10.1016/j.electacta.2022.139892.
[23] J.J. Xue, T. Wu, Y.Q. Dai, Y.N. Xia, Electrospinning and electrospun nanofibers: methods, materials, and applications, Chem. Rev. 119 (2019) 5298–5415, https://doi.org/10.1021/acs, chemrev.8b00593.
[24] D.H. Kong, W. Guo, Y. Zhao, Y. Zhao, Electrospun multiscale structured nanofibers for lithium-based batteries, Adv. Energy Mater. 15 (2025) 2403983, https://doi.org/10.1002/aenm, 202403983.
[25] F. Xie, X. Sheng, Z. Ling, S. Hao, Q. Zhang, M. Sun, G. Liu, F. Diao, Y.Q. Wang, Flexible electrospun iron/manganese-based compounds/carbon fibers: phase transformation and electrochemical properties, Electrochim. Acta 470 (2023) 143288, https://doi.org/10.1016/j.electacta.2023.143288.
[26] A.A. Ensafi, M.M. Abarghoui, B. Rezaei, Metal (Ni and Bi) coated porous silicon nanostructure, high-performance anode materials for lithium ion batteries with high capacity and stability, J. Alloy. Compd. 712 (2017) 233–240, https://doi.org/10.1016/j.jallcom.2017.04.103.
[27] J.J. Wang, X. Sheng, S. Hao, G. Liu, R. Cai, X. Xue, Y.Q. Wang, Construction of $Fe_{0.64}Ni_{0.36}$@graphite nanoparticles *via* corrosion-like transformation from $NiFe_2O_4$ and surface graphitization in flexible carbon nanofibers to achieve strong wideband microwave absorption, J. Colloid Interface Sci. 657 (2024) 193–207, https://doi.org/10.1016/j.jcis.2023.11.145.
[28] J.J. Wang, X.Y. Xue, Y.Q. Wang, Tuning the structural and magnetic properties of electrospun strontium-iron-oxide nanofibers with different stoichiometry, Mater. Charact. 200 (2023) 112884, https://doi.org/10.1016/j.matchar.2023.112884.
[29] H.H. Kang, B.C. Hua, P.Y. Gao, S. Luo, H.R. Yao, Y.Y. Sun, L.Q. Xu, Y.P. Zheng, J. X. Li, Ni/graphdiyne composites inhibit dendrite growth in lithium metal anodes, Electrochim. Acta 440 (2023) 141744, https://doi.org/10.1016/j.electacta.2022.141744.
[30] M. Akter, I. Hossain, M. Howlader, F. Shahriar, U.H. Saima, Recent research advancements in carbon fiber-based anode materials for lithium-ion batteries, Energy Technol. 13 (2025) 2401426, https://doi.org/10.1002/ente.202401426.
[31] A. Yu, Y. Zhao, L.T. Zhu, W.H. Yang, P. Peng, F.-F. Li, In-situ Ni-oxidation-assisted coupling reduction of NiO and CO_2 to synthesize core-shell Ni@octahedral carbon with energy storage properties, Chem. Eng. J. 462 (2023) 142268, https://doi.org/10.1016/j.cej.2023.142268.
[32] J.K. Ou, S.G. Wu, L. Yang, H. Wang, Facile preparation of NiO@graphene nanocomposite with superior performances as anode for Li-ion batteries, Acta Metall. Sin. Engl. Lett. 35 (2022) 212–222, https://doi.org/10.1007/s40195-021-01283-5.
[33] M.J. Xiao, Y. Peng, B. Ma, H. Zhang, X.-Y. Li, Q. Wang, H.-L. Zhang, Hollow NiO/carbon pompons for efficient lithium ion storage, J. Mater. Chem. A 10 (2022) 21492–21502, https://doi.org/10.1039/d2ta05746h.

[34] S.E.T. Siddiqui, M.A. Rahman, J.H. Kim, S.B. Sharif, S. Paul, A review on recent advancements of Ni-NiO nanocomposite as an anode for high-performance lithium-ion battery, Nanomaterials 12 (2022) 2930, https://doi.org/10.3390/nano12172930.
[35] W. Jae, J. Song, J.J. Hong, J. Kim, Raspberry-like hollow Ni/NiO nanospheres anchored on graphitic carbon sheets as anode material for lithium-ion batteries, J. Alloy. Compd. 805 (2019) 957–966, https://doi.org/10.1016/j.jallcom.2019.07.192.
[36] G. Yu, X. Liu, W. Huang, S. Wang, J. Zhan, L. Ma, H. Li, X. Lin, T. Liu, K. Amine, H. Li, Ferromagnetic atomic d-p orbital hybridization for promoting Al-S batteries, Adv. Mater. (2025) 2418784, https://doi.org/10.1002/adma.202418784.
[37] W. Wen, J.M. Wu, M.H. Cao, NiO/Ni powders with effective architectures as anode materials in Li-ion batteries, J. Mater. Chem. A 1 (2013) 3881–3885, https://doi.org/10.1039/C3TA01626A.
[38] Q. Xia, H.L. Zhao, Y.Q. Teng, Z.H. Du, J. Wang, T.H. Zhang, Synthesis of NiO/Ni nanocomposite anode material for high rate lithium-ion batteries, Mater. Lett. 142 (2015) 67–70, https://doi.org/10.1016/j.matlet.2014.11.142.
[39] X.H. Huang, J.P. Tu, C.Q. Zhang, J.Y. Xiang, Net-structured NiO-C nanocomposite as Li-intercalation electrode material, Electrochem. Commun. 9 (2007) 1180–1184, https://doi.org/10.1016/j.elecom.2007.01.014.
[40] X. Li, A. Dhanabalan, K. Bechtold, C. Wang, Binder-free porous core-shell structured Ni/NiO configuration for application of high performance lithium ion batteries, Electrochem. Commun. 12 (2010) 1222–1225, https://doi.org/10.1016/j.elecom.2010.06.024.
[41] L.Q. Xu, X.X. Zhang, R.J. Chen, F. Wu, L. Li, P-doped Ni/NiO heterostructured yolk-shell nanospheres encapsulated in graphite for enhanced lithium storage, Small 18 (2022) 2105897, https://doi.org/10.1002/smll.202105897.
[42] Y. Chen, H.Y. Chen, F.H. Du, X.P. Shen, Z.Y. Ji, H.B. Zhou, A. Yuan, In-situ construction of nano-sized Ni-NiO-MoO_2 heterostructures on holey reduced graphene oxide nanosheets as high-capacity lithium-ion battery anodes, J. Alloy. Compd. 926 (2022) 166847, https://doi.org/10.1016/j.jallcom.2022.166847.
[43] B.N. Zhu, D.D. Liu, L.Y. Wang, B. Zhong, H.P. Liu, Rational design of NiO/$NiSe_2$@C heterostructure as high-performance anode for Li-ion battery, J. Colloid Interface Sci. 643 (2023) 437–446, https://doi.org/10.1016/j.jcis.2023.03.193.
[44] G.Q. Liu, Y.J. Sun, X.G. Guo, C.Z. Yang, Y.W. Cheng, D.M. Liu, Improving charge transfer *via* nickel-nickel oxide/molybdenum dioxide heterostructure for advanced supercapacitor electrode, Electrochim. Acta 478 (2024) 143863, https://doi.org/10.1016/j.electacta.2024.143863.
[45] S.J. Hao, X.L. Sheng, F. Xie, M. Sun, F.Y. Diao, Y.Q. Wang, Electrospun carbon nanofibers embedded with heterostructured $NiFe_2O_4/Fe_{0.64}Ni_{0.36}$ nanoparticles as an anode for high-performance lithium-ion battery, J. Energy Storage 80 (2024) 110412, https://doi.org/10.1016/j.est.2023.110412.
[46] F. Xie, M. Sun, X.L. Sheng, Q.Y. Zhang, Z.B. Ling, S.J. Hao, F.Y. Diao, Y.Q. Wang, Graphene-wrapped Fe_2TiO_5 nanoparticles with enhanced performance as lithium-ion battery anode, Mater. Lett. 358 (2024) 135877, https://doi.org/10.1016/j.matlet.2024.135877.
[47] L. Zhang, F. Xie, S. Hao, F.Y. Diao, Y.Q. Wang, Annealing condition engineering of electrospun iron-titanium oxide nanofibers for enhanced lithium storage performance, Electrochim. Acta 536 (2025) 146746, https://doi.org/10.1016/j.electacta.2025.146746.
[48] S.J. Hao, B. Zhang, Q. Zhang, M. Sun, R.S. Cai, F.Y. Diao, Y.Q. Wang, Effectiveness of three distinct strategies of constructing ZnO-based composites for enhanced electrochemical performance, J. Phys. Chem. Solids 211 (2026) 113502, https://doi.org/10.1016/j.jpcs.2025.113502.
[49] M. Sun, G.T. Liu, S.J. Hao, F.Y. Diao, F. Rosei, R.S. Cai, Y.Q. Wang, Correlation between spinel structure and electrochemical kinetic behavior of spinel ferrites, J. Electroanal. Chem. 1005 (2026) 119870, https://doi.org/10.1016/j.jelechem.2026.119870.
[50] M. Chen, M.Y. Zhao, K. Liu, F.M. Liu, Z.Y. Yuan, X. Qian, R. Wan, C.S. Li, A.X. Ding, Structural reconstruction via carbon nanotube spatially confined metal catalysis: a morphology-controlled approach to convert polycyclic aromatic hydrocarbon into carbon nanofibers for highly active anodes in Li-Ion batteries, Inorg. Chem. 64 (2025) 3594–3607, https://doi.org/10.1021/acs.inorgchem.4c05514.
[51] M. Chen, F.M. Liu, M.Y. Zhao, X. Qian, L. Liu, R. Wan, Z.Y. Yuan, C.S. Li, Q.Y. Niu, Rational synthesis of spongy Fe_3N@N-doped carbon nanorods with controlled topography and porosity for enhanced energy storage anodes in lithium-ion batteries, Langmuir 40 (2024) 24017–24028, https://doi.org/10.1021/acs.langmuir.4c03305.
[52] M. Chen, M.Y. Zhao, F.M. Liu, M.T. Li, M.L. Zhang, X. Qian, Z.Y. Yuan, C.S. Li, R. Wan, Self-catalyzed synthesis of length-controlled one-dimensional nickel oxide@N-doped porous carbon nanostructures from metal ion modified nitrogen heterocycles for efficient lithium storage, Langmuir 40 (2024) 4852–4859, https://doi.org/10.1021/acs.langmuir.3c03742.
[53] F.M. Liu, M.Y. Zhao, S. Wang, M. Chen, X. Qian, Z.Y. Yuan, Y. Sun, C.S. Li, R. Wan, A new synthesis strategy for nitrogen-doped carbon nanofibers with cobalt oxide nanoparticles as anodic electrode materials for lithium ion batteries, Chem. Commun. 59 (2023) 12771–12774, https://doi.org/10.1039/D3CC04394K.
[54] M. Chen, F.M. Liu, S.S. Chen, X. Qian, Y.J. Zhao, Y. Sun, C.S. Li, R. Wan, Z.Y. Yuan, Low-temperature metal-catalyzed synthesis of encapsulated metal oxide nanoparticles in nitrogen-doped carbon nanotubes from carbon nitride as anodic materials of high-performance lithium-ion batteries, N. J. Chem. 47 (2023) 3215–3221, https://doi.org/10.1039/D2NJ05948G.
[55] M. Chen, F.M. Liu, S.S. Chen, R. Wan, X. Qian, Z.Y. Yuan, Cactus-like iron oxide/carbon porous microspheres lodged in nitrogen-doped carbon nanotubes as anodic electrode materials of lithium ion batteries, N. J. Chem. 47 (2023) 765–771, https://doi.org/10.1039/D2NJ05404C.
[56] M. Chen, F.M. Liu, H. Zhao, S.S. Chen, X. Qian, Z.Y. Yuan, R. Wan, In situ encapsulation of iron oxide nanoparticles into nitrogen-doped carbon nanotubes as anodic electrode materials of lithium ion batteries, Phys. Chem. Chem. Phys. 24 (2022) 27114–27120, https://doi.org/10.1039/D2CP04228B.
[57] M. Chen, L.L. Shao, X.Q. Wang, X. Qian, Z.Y. Yuan, L.X. Fang, A.X. Ding, X.W. Lv, Y.N. Wang, Controlled synthesis of highly active nonstoichiometric tin phosphide/carbon composites for electrocatalysis and electrochemical energy storage applications, ACS Sustain. Chem. Eng. 10 (2022) 1482–1498, https://doi.org/10.1021/acssuschemeng.1c06699.
[58] M. Chen, Q.S. Jing, H.B. Sun, J.Q. Xu, Z.Y. Yuan, J.T. Ren, A.X. Ding, Z.Y. Huang, M.Y. Dong, Engineering the core–shell-structured NCNTs-Ni_2Si@Porous Si composite with robust Ni–Si interfacial bonding for high-performance Li-Ion batteries, Langmuir 35 (2019) 6321–6332, https://doi.org/10.1021/acs.langmuir.9b00558.
[59] M.Y. Zhao, F.M. Liu, M. Chen, X. Zhang, X. Qian, Z.Y. Yuan, R. Wan, C.S. Li, W. X. Yue, Controlled synthesis of Fe_3N sandwiched in nitrogen-doped multilayer graphene as an anode material for lithium-ion batteries, ACS Appl. Energy Mater. 8 (2025) 12769–12779, https://doi.org/10.1021/acsaem.5c01871.
[60] F. Zheng, S. Xu, Y. Zhang, Facile fabrication of hierarchically porous NiO microspheres as anode materials for lithium ion batteries, J. Mater. Sci. Mater. Electron. 27 (2016) 3576–3582, https://doi.org/10.1007/s10854-015-4194-6.
[61] C. Luo, Z. Wang, Y. Chen, Y. Zhao, Q. Han, C. Qin, Z. Wang, Eutectic-derived bimodal porous Ni@NiO nanowire networks for high-performance Li-ion battery anodes, Int. J. Energy Res. 46 (2022) 24654–24666, https://doi.org/10.1002/er.8711.
[62] Y. Song, J. Hwang, S. Lee, B. Thirumalraj, J.-H. Kim, P. Jenei, J. Gubicza, H. Choe, Synthesis of a high-capacity NiO/Ni foam anode for advanced lithium-ion batteries, Adv. Eng. Mater. 22 (2020) 2000351, https://doi.org/10.1002/adem.202000351.
[63] C. Luo, W. Lu, Y. Li, Y. Feng, W. Feng, Y. Zhao, X. Yuan, Preparation of C/Ni-NiO composite nanofibers for anode materials in lithium-ion batteries, Appl. Phys. A 113 (2013) 683–692, https://doi.org/10.1007/s00339-013-7700-9.
[64] G. Li, Y. Li, J. Chen, P. Zhao, D. Li, Y. Dong, L. Zhang, Synthesis and research of egg shell-yolk NiO/C porous composites as lithium-ion battery anode material, Electrochim. Acta 245 (2017) 941–948, https://doi.org/10.1016/j.electacta.2017.06.039.
[65] J. Liu, T. Gu, L. Li, L. Li, Synthesis of MnO/C/NiO-doped porous multiphasic composites for lithium-ion batteries by biomineralized Mn oxides from engineered pseudomonas putida cells, Nanomaterials 11 (2021) 361, https://doi.org/10.3390/nano11020361.